

# Journal of Materials Chemistry A

Accepted Manuscript



This is an *Accepted Manuscript*, which has been through the Royal Society of Chemistry peer review process and has been accepted for publication.

*Accepted Manuscripts* are published online shortly after acceptance, before technical editing, formatting and proof reading. Using this free service, authors can make their results available to the community, in citable form, before we publish the edited article. We will replace this *Accepted Manuscript* with the edited and formatted *Advance Article* as soon as it is available.

You can find more information about *Accepted Manuscripts* in the [Information for Authors](#).

Please note that technical editing may introduce minor changes to the text and/or graphics, which may alter content. The journal's standard [Terms & Conditions](#) and the [Ethical guidelines](#) still apply. In no event shall the Royal Society of Chemistry be held responsible for any errors or omissions in this *Accepted Manuscript* or any consequences arising from the use of any information it contains.

Cite this: DOI: 10.1039/c0xx00000x

www.rsc.org/xxxxxx

ARTICLE TYPE

## Facile synthesis of Pd nanostructures in hexagonal mesophases as promising electrocatalyst for ethanol oxidation

Srabanti Ghosh<sup>a,b\*</sup>, Hynd Remita<sup>b,c</sup>, Prasenjit Kar<sup>a</sup>, Susobhan Choudhury<sup>a</sup>, Samim Sardar<sup>a</sup>, Patricia Beaunier<sup>d</sup>, Partha Sarathi Roy<sup>e</sup>, Swapan Kumar Bhattacharya<sup>e</sup>, Samir Kumar Pal<sup>a</sup>

Received (in XXX, XXX) Xth XXXXXXXXX 20XX, Accepted Xth XXXXXXXXX 20XX

DOI: 10.1039/b000000x

One of the significant challenges for the commercialization of direct ethanol fuel cells (DEFCs) is the preparation of active, robust, and low-cost catalysts. In this work, a facile and reproducible method is demonstrated for the synthesis of Pd assembled nanostructures in a hexagonal mesophase formed by a quaternary system (Pd-doped water, surfactant, oil, and cosurfactant) *via* photo irradiation. The formation of Pd nanostructures in the confined region of hexagonal mesophases further supported with water relaxation dynamics study using solvation probe. The mesophases can be doped by high concentrations of palladium salt (0.1 M) without any disturbance of the structure of the mesophases which allows the high yield and clean synthesis of Pd nanostructures without using any toxic chemicals. Electrochemical measurement confirms that the as-prepared catalysts exhibit significant electrocatalytic activity for the ethanol oxidation in alkaline solution. Additionally, we present an alternative strategy using reduced graphene oxide nanosheets in combination with nafion (a proton conducting phase) as a support, revealing the pronounced impact on dramatically enhanced electrocatalytic activity and stability of Pd nanostructures compared to nafion alone. This unique combination allowed the effective dispersion of the Pd nanostructures that is connected with an enhancement of the catalytic activity. Our approach paves the way towards the rational design of practically relevant catalysts with both the enhanced activity and durability of electrocatalysts for fuel cell applications.

### 1. Introduction

The development of advanced materials and processes is a central issue which contributes to the ultimate goal to accelerate the implementation of novel nanomaterials-based technology providing clean and affordable energy.<sup>1-3</sup> Platinum is the superlative electrocatalyst for most of the relevant reactions involved in fuel cells which constitute promising future power sources. However, several critical issues such as the migration, aggregation and dissolution in harsh electrochemical environments as well as the weak CO poisoning tolerance, high cost must be resolved before Pt-based electrocatalysts can be commercialized.<sup>4, 5</sup> Alternatively, Pd based nanostructured materials play a crucial role in the catalysis of various relevant reactions in fuel cells, resulting in enhanced intrinsic electroactivity with high energy conversion efficiency, which is suitable for direct ethanol fuel cells (DEFCs).<sup>6-8</sup> Therefore, many recent efforts have been devoted to control the morphology and composition of Pd-based catalysts that can offer a great opportunity to achieve enhanced catalytic performance and higher utilization of Pd.<sup>9-14</sup> In our earlier reports, Pd nanowires, and porous Pd nanoballs connected with three-dimensional Pd nanowires demonstrated superior electro-catalytic activity for the ethanol oxidation and appear as promising candidates for fuel cell applications.<sup>15, 16</sup> In spite of these successful demonstrations, it is important to note that their mass activity (in terms of Pd) for the

ethanol electrooxidation is still not satisfactory.<sup>17-19</sup> Hence, it is highly desirable to develop a simple method for the synthesis of novel Pd nanoparticles (NPs) based electrocatalysts with high activity and durability for fuel cell applications. Moreover, various shape-controlled Pd nanostructures have been extensively explored for electrocatalysis. Nevertheless, the reports regarding self-assembled Pd nanostructures are scarce. Herein, we demonstrate a very simple and efficient route to synthesize Pd nanostructures in liquid crystals by photoreduction.

Liquid crystal (LC) appears as perfect candidates for the matrix-guided synthesis and self-assembly of nanoscale materials as it combines order and mobility at the molecular (nanoscale) level.<sup>20-23</sup> Few examples have been reported for the preparation of nanostructures in nematic LC as structure-directing templates.<sup>22, 24</sup> One of the significant problems of templating of nematic domains is that nanoparticles expelled to domain boundaries which lead to the formation of particulate networks and consequently, free-standing porous materials can not achieved using this route.<sup>25-27</sup> Attard et al. successfully demonstrated that direct hexagonal LCs made by a ternary mixture (nonionic surfactant, metal salts, and water) can be used as template for the synthesis of bulk porous materials and porous metal films by electro-deposition.<sup>28, 29</sup> Recently, we reported a systematic study of the effect of templating approach allowing the synthesis of bimetallic nanoballs of tunable porosity and composition in a swollen hexagonal mesophase (SLC).<sup>30</sup> The swollen mesophases

consist of surfactant-stabilized oil-swollen tubes that are arranged on a triangular lattice in an aqueous medium.<sup>31, 32</sup> In the past years, we employed doped SLC with various compounds and used as nanoreactors to synthesize diverse nanostructured materials (such as metal, polymer or oxides) both in the aqueous and in the oil phases.<sup>33-36</sup> Here, the photoreduction of palladium salt is induced by UV light irradiation within the aqueous phase of hexagonal mesophases. By virtue of having Pd as an active electrocatalyst, we studied the ethanol oxidation reaction (EOR) using as prepared Pd nanostructures as the anode material. Additionally, in order to enhance the dispersion and accessibility of catalyst reduced graphene oxide nanosheets (RGO) modified Pd nanostructure has been used in combination with Nafion support during electrooxidation.

Despite the immense advances in unsupported nanostructured noble metals as electrocatalysts, the relatively low efficiency and high usage of noble metals in such unsupported metal catalysts still limit their practical applications. Hence, design and fabrication of more active electrocatalysts with excellent performance, durability and low cost are of great importance. To improve the electrochemical performance of these catalysts, carbon based conductive substrates such as carbon nanotubes (CNT), carbon fibers and Vulcan XC-72 (VXC) etc are widely used as supports to disperse the metal NPs.<sup>37-40</sup> Supported metal NPs play a pivotal role as catalysts for energy storage/conversion, however, the aggregation tendency of NPs is an impediment for stable performance and loss of active surface area is a major cause of deactivation for supported catalysts.<sup>41, 42</sup> Recently, we demonstrated that the utilization of conducting polymer nanostructures improve the electrocatalytic activity and durability of Pd catalysts.<sup>43</sup> A good catalyst support should possess good conductivity and mechanical strength, long term stability with high surface area.<sup>44, 45</sup> In this respect, graphene oxides possess high surface area, low cost and enhanced conductivity, and they have been chosen as excellent carbon supports for catalysts to achieve enhanced electrochemical performance for fuel oxidation, oxygen reduction and water splitting reactions.<sup>46-49</sup> With the ease of processibility and functionalization make graphene-based functional materials ideal candidates for a variety of energy applications.<sup>50, 51</sup> Hence, reduced RGO nanosheets in combination with nafion can be used as an efficient support for metal NPs and would exhibit fascinating catalytic properties. We report the synthesis and characterization of assembled palladium nanostructures in hexagonal mesophases. We demonstrate that the Pd nanostructures synthesized in soft templates are promising electrocatalysts having superior activity and stability for EOR. Moreover, the introduction of RGO nanosheets along with nafion into the electrode containing the Pd nanostructures leads to high electrocatalytic activity and durability for EOR.

## 2. Experimental

**2.1 Reagents** Pd(NH<sub>3</sub>)<sub>4</sub>Cl<sub>2</sub> (99% purity), cetylpyridinium chloride (CPCI, 98% purity), sodium chloride, cyclohexane (>99%), pentanol (≥99%), 5 wt% nafion solution, coumarin (C500) and 4-(dicyanomethylene)-2-methyl-6-(p-dimethylamino-styryl) 4H-pyran (DCM), graphite powder, 2-propanol and ethanol were purchased from Sigma-Aldrich. All compounds were used as received. Ultrapure water (Millipore System, 18.2 MΩ cm) and ethanol (≥ 99% for HPLC, purchased from Sigma-Aldrich) were used as solvents.

**2.2 Preparation of Catalyst:** The swollen hexagonal mesophases with CPCI as surfactant were prepared following the previously published method with some modifications.<sup>31, 35</sup> Typically, 1 g of the surfactant (CPCI) was dissolved in 2 mL of brine (an aqueous

solution containing 0.1 mol.L<sup>-1</sup> NaCl or 0.1 mol.L<sup>-1</sup> Pd(NH<sub>3</sub>)<sub>4</sub>Cl<sub>2</sub> in pyrex glass tubes. After a vigorous agitation at 30°C, the surfactant had completely dissolved to give a transparent and viscous micellar solution. The subsequent addition of cyclohexane in the micellar solution under stirring leads to a white unstable emulsion. A cosurfactant, pentanol-1 was added to the mixture, which was then strongly vortexed for a few minutes. This led to a perfectly colorless, translucent, birefringent and stable gel: a hexagonal mesophase. All experiments were performed at room temperature. The doped mesophases with the Pd salt were used as soft templates to synthesize palladium nanostructures induced by irradiation by UV light. For *in-situ* photoreduction, the doped mesophases were transferred in quartz cells and irradiated with an Oriol 300 W Xenon UV-visible lamp at a distance of 5 cm for 12 hours. After reaction, the metal NPs were easily extracted from the mesophases by a simple washing process with 2-propanol, centrifuged, and washed several times to remove the surfactant, the cosurfactant and the salt. For solvation dynamics study, we doped hexagonal mesophases with two common salivation probes such as coumarin (C500) and 4-(dicyanomethylene)-2-methyl-6-(p-dimethylamino-styryl) 4H-pyran (DCM).

The graphene used here was prepared with the modified Hummer method.<sup>52, 53</sup> Firstly, 1 g of graphite, 0.5 g of NaNO<sub>3</sub> and 30 mL of H<sub>2</sub>SO<sub>4</sub> (98 wt%) were added into a flask with stirring in an ice bath. Then 3.0 g of KMnO<sub>4</sub> was added gradually in one hour. After cooling, the mixture was continually stirred at room temperature for 3 days. The mixture was then slowly added into 100 mL of 5 wt% H<sub>2</sub>SO<sub>4</sub> in one hour under stirring. After another two hours of stirring, 2.7 mL of 30 wt% H<sub>2</sub>O<sub>2</sub> was added into the mixture and stirred again for two more hours. The mixture was then filtered and washed with a solution of 0.5 wt% H<sub>2</sub>O<sub>2</sub> and 3 wt% H<sub>2</sub>SO<sub>4</sub> for several times. Finally, the mixture was washed with distilled water to remove residual metal ions and acid. The product graphene oxide (GO) was dried in air. The GO (mg/mL) was then dispersed in 2-propanol and exfoliated in an ultrasonic bath followed by deoxygenated under a N<sub>2</sub> flow. The GO sample was then exposed to  $\gamma$ -irradiation at room temperature for 10 h (irradiation dose of 6.4 kGy) under N<sub>2</sub> atmosphere. The  $\gamma$ -irradiation source, located at Orsay, was a panoramic <sup>60</sup>Co gamma-facility of 7000 Curies with a maximum dose rate of 6400 Gy. h<sup>-1</sup>. After reaction, the reduced GO was centrifuged, and washed several times with ethanol.

### 2.3 Material Characterization:

Transmission electron microscopy (TEM) observations were performed using an FEI (Technai S-Twin, operating at 200 kV) instrument and with a JEOL 100CXII transmission electron microscope at an accelerating voltage of 100 kV. Drops of the Pd nanostructures in ethanolic solutions were deposited on carbon coated copper grids and dried under a N<sub>2</sub> flow. XRD patterns were obtained by employing a scanning rate of 0.02° S<sup>-1</sup> in the 2 $\theta$  range from 20° to 80° by a PANalytical XPERTPRO diffractometer equipped with Cu K $\alpha$  radiation (at 40 mA and 40 kV). Optical microscopy of gel samples before and after polymerization was performed with a Leica DMRX polarizing microscope. For optical experiments, the steady-state absorption and emission were determined with a Shimadzu UV-2450 spectrophotometer and a Jobin Yvon Fluoromax-3 fluorimeter respectively. Picosecond-resolved fluorescence decay transients were measured by using a commercially available spectrophotometer (Life Spec-ps, Edinburgh Instruments, UK) with 70 ps instrument response function (IRF). The excitation at 375 nm and 409 nm were obtained using pulse laser diodes from PicoQuant, Germany. The observed fluorescence transients were fitted by using a nonlinear least square fitting procedure to a

function  $(X(t) = \int_0^t E(t')R(t-t')dt')$  comprising of

convolution of the IRF ( $E(t)$ ) with a sum of exponential

$(R(t) = A + \sum_{i=1}^N B_i e^{-t/\tau_i})$  with pre-exponential factors ( $B_i$ ),

characteristic lifetimes ( $\tau_i$ ) and a background ( $A$ ). Relative

concentration in a multi exponential decay was finally expressed

as:  $C_n = \frac{B_n}{\sum_{i=1}^N B_i} \times 100$ . The quality of the curve fitting was

evaluated by reduced chi-square and residual data. It has to be

noted that with our time-resolved instrument, we can resolve at

least one fourth of the instrument response time constants after

the de-convolution of the IRF. The average lifetime (amplitude-

weighted) of a multi-exponential decay is expressed

as:  $\tau_{av} = \sum_{i=1}^N C_i \tau_i$ . Time-resolved emission spectrum (TRES)

were used to construct time-dependent fluorescence Stokes

shifts.<sup>54, 55</sup> The time-dependent fluorescence Stokes shifts, as

estimated from TRES, are used to construct the normalized

spectral shift correlation function or the solvent correlation

function,  $C(t)$ , defined as,  $C(t) = \frac{v(t) - v(\infty)}{v(0) - v(\infty)}$ , where  $v(0)$ ,  $v(t)$ ,

and  $v(\infty)$  are the emission maxima (in  $\text{cm}^{-1}$ ) at time 0,  $t$ , and  $\infty$

respectively. The  $v(\infty)$  value corresponds to the emission

frequency beyond which is not significant or no spectral shift is

observed. The  $C(t)$  function represents the temporal response of

the solvent relaxation process. Anisotropy  $r(t)$  is defined as,

$r(t) = \frac{I_{para} - I_{per}}{I_{para} + 2 \times I_{per}}$  where  $I_{para}$  is emission intensity taken

at parallel to that of the excitation and  $I_{per}$  is that of in the

perpendicular position. Fourier transformed infrared spectroscopy

(FTIR) of solid Pd salt and solid Pd NPs powders as synthesized

by UV irradiation (obtained after extraction from the

mesophases) were recorded using a JASCO FTIR-6300

spectrometer. Scanning wavelengths were varied from 4000–600

$\text{cm}^{-1}$  with a  $2 \text{ cm}^{-1}$  spectral resolution with 100 repetitions scans

average for each spectrum.

The Pd content deposited on the electrode (see next section)

was determined by inductively coupled plasma-mass

spectrometry (ICP-MS) as follows: i) the solvent was first

evaporated; ii) samples were mineralized using 5 mL of aqua

regia and injected, after a 20 times dilution with ultrapure water,

via a peristaltic pump at  $0.1 \text{ mL min}^{-1}$  flow rate; iii) nebulization

of samples was performed by means of a microconcentric

nebulizer (Micromist); iv) a 7500 ce ICP-MS (Agilent) was used

as elemental detector. Detection of Pd was performed by

selecting an abundant isotope free of interferences, i.e.,  $^{105}\text{Pd}$ .

**2.4 Electrochemical characterization:** The electrochemical

measurements were conducted at  $30^\circ\text{C}$  in a two compartment

glass-cell fitted with a conventional three electrode assembly. In

all electrochemical measurements, a glassy carbon rod used as

working electrode and Hg/HgO/OH (1 M) (designated as MMO)

having an equilibrium electrode potential of  $\sim 0.1 \text{ V}$  with respect

to the standard hydrogen electrode (SHE). A large Pt-foil ( $1 \text{ cm}$

$\times 1 \text{ cm}$ ) was used as counter electrode and potential data were

recorded with respect to MMO. Cyclic voltammetric study was

performed using a computer aided Potentiostat/Galvanostat

(AEW-2, Munistst, Sycopel Scientific Ltd., UK). Cyclic

voltammogram (CV) of each electrode was recorded at the scan

rate  $50 \text{ mVs}^{-1}$  for several consecutive cycles until a steady profile

was obtained. Chronopotentiometry was also performed by

applying a current density of  $5 \text{ mA cm}^{-2}$  with the help of a

constant current charger (DB-300, DB – Electronics) and the

potential was recorded with an EC digital multimeter (DM 610

4B) as described before.<sup>56</sup> The glassy carbon electrode was

pretreated using the following process. First, the surface of a

glassy carbon electrode was polished with 1.0, 0.3 and  $0.05 \mu\text{m}$

$\alpha$ -alumina powders in sequence, rinsed thoroughly with twice

distilled water and placed in a water-filled ultrasonic bath over a

2 min period. After dried in air, Pd NPs were deposited for

further use.

Pd nanostructure suspension consisting of  $0.5 \text{ mg}$  of Pd NPs

in  $500 \mu\text{L}$  of  $0.5 \%$  wt nafion (as Pd/Nafion) and another

suspension consisting of  $0.25 \text{ mg}$  of Pd NPs with  $0.25 \text{ mg}$

reduced GO nanosheets (RGO) in  $500 \mu\text{L}$  of  $0.5 \%$  wt nafion

(Pd/RGO-Nafion) in ethanol solution were used for the

electrochemical characterization. A layer was prepared by

depositing  $10 \mu\text{L}$  of the homogeneous solution of Pd NPs

suspensions on a polished glassy carbon electrode surface.

The above suspensions were used for the determination of Pd

content by ICP-MS and the amount of palladium on the glassy

carbon for nafion and RGO-nafion is  $4.9 \mu\text{g}$  and  $2.48 \mu\text{g}$

respectively. The layer was allowed to dry for at least 60 min.

The Pd/RGO-Nafion is not directly deposited on the electrode

surface but they are embedded within the nafion and RGO-nafion

### 3. Results and Discussion

Swollen hexagonal mesophases, resulting from the surfactant

mediated self-assembly in a quaternary system (water, surfactant,

cosurfactant, and oil) serves as versatile templates for

synthesizing various nanomaterials.<sup>31, 35</sup> For Pd nanostructure

synthesis, we prepared mesophases doped with  $0.1 \text{ M}$  Pd

complex with a volume ratio of oil over water (O/W) (v/v) fixed

at 1.5 for the *in-situ* photo reduction. The Pd nanostructures

synthesized in doped CPCl-based mesophases were extracted

with 2-propanol. Fig.1 shows the UV-Vis spectra of Pd ( $\text{NH}_3$ )<sub>4</sub>Cl<sub>2</sub>

complex (solid black line) and the suspensions of the Pd

nanostructure (solid red line) extracted from mesophases after 12

hours of photoirradiation. The Pd complex showed a peak at 297

nanostructures.<sup>59, 60</sup> Typically, the formation of Pd nanoparticles via chemical or photochemical route is indicated by the emergence of black color. The Pd complex doped mesophases remains colorless and upon photoirradiation, turns to a black color gel after 12 hours but remains translucent (Fig. 1 inset). In fact, immediately after photo irradiation, hexagonal mesophases turns into faint black gel but with the progress of reduction of Pd (II) are indicated by the increase in the darkness of the gel.

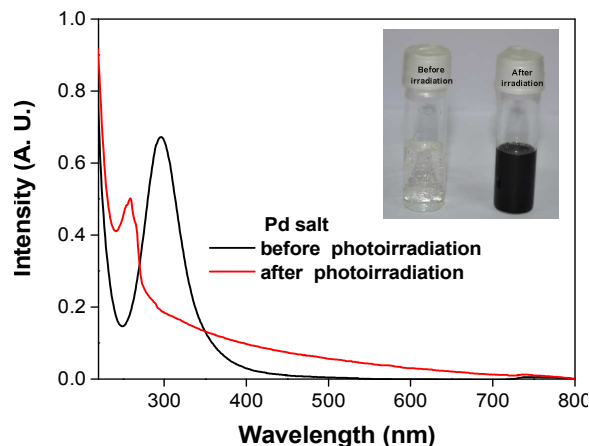


**Fig. 1** UV-visible spectra of Pd (NH<sub>3</sub>)<sub>4</sub>Cl<sub>2</sub> complex before and after photo irradiation. Inset: Photographs of hexagonal mesophases doped with 0.1 M Pd (NH<sub>3</sub>)<sub>4</sub>Cl<sub>2</sub> complex before and after UV irradiation exposure. The color change indicates the photo reduction of Pd complex by UV irradiation.

After photoreduction of the Pd complex within the hexagonal mesophases, it is important to ensure the stability of hexagonal mesophases in order to understand the effect of confinement. The hexagonal phases are birefringent and exhibit characteristic textures between crossed polarizing windows when the surfactant cylinders are parallel to the walls of the observation cell. The polarized optical microscopy image (Fig. S2a-d) demonstrates that the presence of Pd complex (Fig. S2b) and photo induced chemical transformation (Fig. S2c-d) does not affect the birefringent nature of the gels nor their texture. After photo reduction of the Pd complex, the hexagonal LC phase shows a large degree of preservation of the birefringent pattern indicative of their stability. The photoreduction of the Pd complex in hexagonal mesophases leads to Pd nanostructures as shown in Fig. 2.

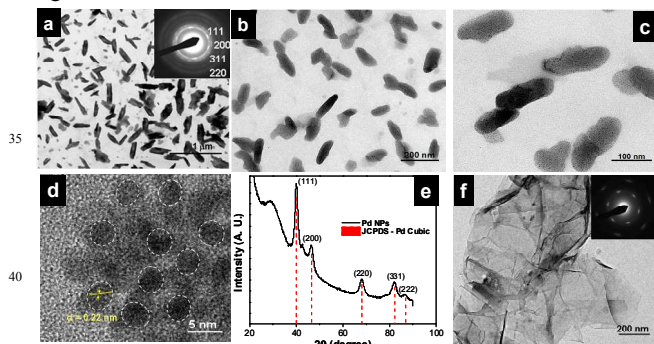


**Fig. 2** Transmission electron micrographs of (a-c) Pd nanostructures synthesized in hexagonal mesophases by 12 h UV-irradiation. The inset shows the indexed corresponding SAED pattern. (d) HRTEM high magnification image of palladium nanoparticles. (e) XRD patterns of palladium nanoparticles with

JCPDS (05-0681) data. (f) Reduced graphene oxides nanosheets induced by gamma ( $\gamma$ )-irradiation (dose rate: 6.4 kGy h<sup>-1</sup>, at dose of 64 kGy) using a solution containing graphene oxides in 2-propanol under N<sub>2</sub> atmosphere. The inset: SAED pattern of graphene oxide nanosheets.

The as prepared Pd nanostructures assembled together as prolate ellipsoids-like structures composed of self assembly of small Pd nanoparticles (NPs) of 3-4 nm in size (Fig. 2a-c). A magnified image (Fig. 2b-c) reveals that the nanoparticles have a narrow size distribution and are well dispersed. It can be clearly seen that the prolate ellipsoids-like nanostructures are formed by the agglomeration of smaller Pd nanoparticles. This can be assumed that after template removal, the nanoparticles are close in contact and their inter particle interaction may contribute this assembled structure. The selected area electron diffraction (SAED) pattern recorded from one of the Pd nanostructures (Inset of Fig. 2a) shows diffraction rings corresponding to various facets of cubic (fcc) crystal structure of palladium. The HRTEM image (Fig. 2d) further confirms that each nanostructure is composed of many single crystalline grains (see white dashed circles in Fig. 2d with their crystallographic orientations). The inter-planar distance in the lattice fringes of one domain is measured to be 0.22 nm (inset), which corresponds to the (111) planes of metallic Pd.

The XRD pattern of the typical product is presented in Fig. 2e. The broad diffraction peaks are present at  $2\theta = 40.6^\circ, 46.6^\circ, 68.4^\circ, 82^\circ$  and  $87^\circ$  and can be indexed as the (111), (200), (220), (311) and (222) facets diffractions of face-centered cubic (fcc) Pd (JCPDS No 05-0681), respectively. This indicates that the Pd NPs have a high purity and crystallinity. Both the XRD and SAED patterns demonstrate that the Pd nanostructures are well crystallized. Time evolution of Pd nanostructures implied that small Pd particles generated at the early stage of the reaction by fast reduction *via* the particle attachment growth mechanism (Fig. S3). The dendritic Pd nanostructures seem to be assembled from many small Pd NPs in the range of 3-4 nm.

Fig. 2e shows the TEM image of reduced graphene oxides (RGO) which exhibit typical wrinkled and paper-like sheets morphologies with a mixture of single and few-layer graphene nanosheets. The corrugation and scrolling of sheets obtained here is the intrinsic nature of graphene, which may originated from the thermodynamic stabilization of the 2D membrane structures via bending. Fig. 2e: inset depicts the SAED pattern of RGO, which clearly demonstrates a highly crystalline structure. The six membered inner rings originate from the [100] plane, while the six brilliant points relate to the [110] diffractions, clearly confirming that the resulting RGO has been restored into the hexagonal graphene framework (Images at higher resolutions and layered morphologies are shown in the Fig. S4).<sup>61</sup> The ability to produce graphene nanosheets with a scalable, clean without using any chemical reducing agent via low-cost approach should take us a step closer to real-world applications of graphene.

The control experiment carried out in micellar solutions formed by CPCI containing Pd(NH<sub>3</sub>)<sub>4</sub>Cl<sub>2</sub> (with the same ratio [CPCI]/[Pd] = 14). The photoreduction of Pd complex leads in this case to the formation of small and spherical dispersed nanoparticles of 3-5 nm (Fig. 3). Additionally, Pd complex doped hexagonal mesophases kept in the dark for several days but there was no sign of evolution of Pd (0). Under UV irradiation, Pd(II) is reduced at the oil-water interface.<sup>33, 62</sup> Initially, nuclei are formed and then they tend to aggregate to form bigger particles or successive reduction of Pd (II) may adsorb on the surface of preformed particles. In this regard, surfactant molecules protect the metal clusters and control the aggregation via hydrophobic

chain mediated electrostatic repulsion and steric hindrance. However, it is intricate to convey the exact mechanism of formation of prolate ellipsoids-like structures within the hexagonal mesophases.

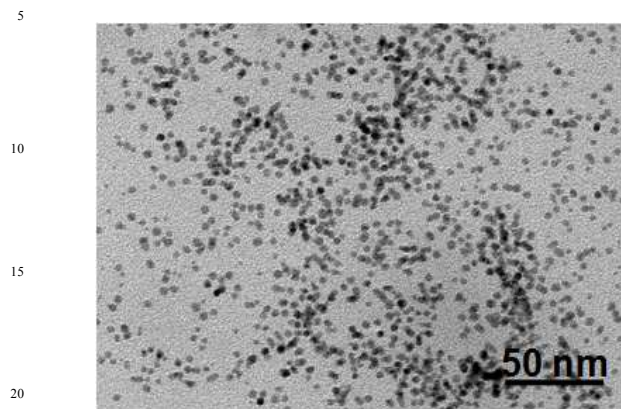
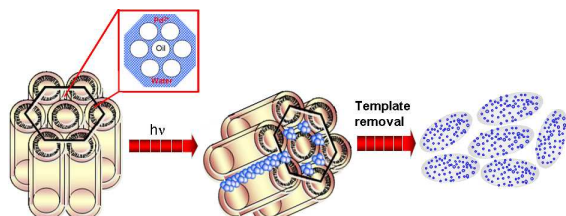


**Fig. 3** TEM micrographs of Pd nanoparticles obtained from the micellar solution of CPCI containing  $\text{Pd}(\text{NH}_3)_4\text{Cl}_2$  ( $[\text{CPCI}]/[\text{Pd}] = 14$ ) at 12 hours photo-irradiation.

The confined geometry of mesophases is certainly involved directing the nanoparticle growth leading to these assembled Pd nanostructures. The hexagonal mesophases consist of infinite nonpolar tubes organized on a hexagonal lattice with surfactants at the interface of the tubes in a continuous aqueous salt solution. It has been demonstrated that the suitable correct adjustment between cyclohexane and the ionic force of the aqueous solution by addition of a salt allowed the diameter of the nonpolar cylinders to be tuned over 1 order of magnitude (from 3 to 30 nm), while the distance between adjacent cylinders is kept small and nearly constant (about 3 nm).<sup>21, 32</sup> Here, we demonstrate that the confined aqueous phase can be used as nanoreactors for the preparation of Pd nanostructures as shown in scheme 1.



**Scheme 1** Schematic representation of light induced synthesis of Pd nanostructures in hexagonal mesophases.

In order to shed light on the mechanism of formation of Pd nanostructures within the confined geometry of hexagonal mesophases, we studied the solvation dynamics in the water surface and hydrophobic region of oil tube of the LC followed by doping with solvation probe such as coumarin 500 (C500) and 4-(dicyanomethylene)-2-methyl-6-(p-dimethylamino-styryl) 4H-pyran (DCM) respectively. The picosecond resolved fluorescence transients of C500 and DCM in mesophases across the emission wavelengths are shown in Fig. 4a and 4b respectively. An ultrafast decay component in the blue end is eventually converted in to a rise component of similar time constant in both the cases. The observation is consistent with the solvation probe C500 and DCM in the corresponding medium.<sup>63, 64</sup> Fig. 4c and 4d show the constructed time-resolved emission spectra (TRES) of C500 and DCM with a spectral shift of 1790 and 2268  $\text{cm}^{-1}$  respectively, in a 1.4 ns time window, which indicate that both probes are stabilized by the corresponding immediate solvent molecules in

the excited state. To determine the water relaxation dynamics within the hexagonal mesophases, we composed solvation correlation functions  $[C(t)]$  for both probe C500 and DCM and fitted with bi-exponential decay function as shown in Fig. 4e and 4f.

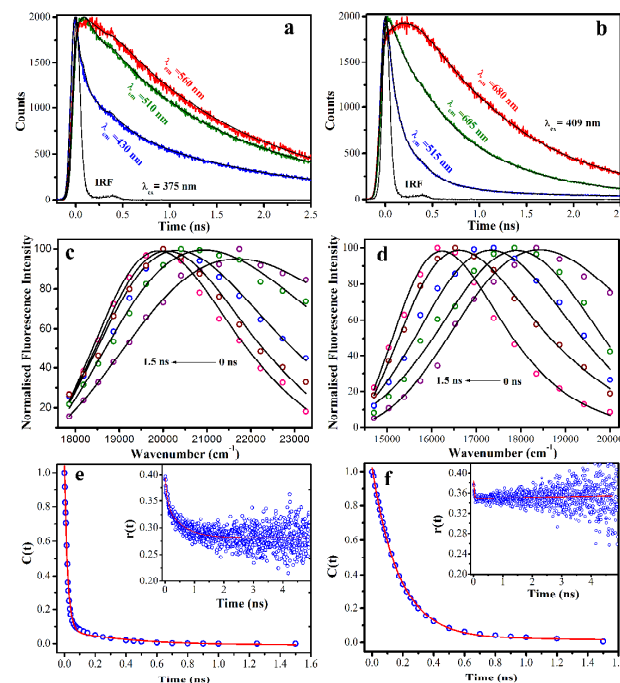


**Fig. 4** Picosecond resolved fluorescence transients of (a) C500 and (b) DCM in three representative detection wavelengths across the emission spectrum in hexagonal mesophases. Time dependent emission spectra of (c) C500 and (d) DCM in the liquid crystal are shown. Plot of solvation correlation functions against time for (e) C500 and (f) DCM are shown. Insets depict the picosecond fluorescence anisotropy decays of C500 and DCM.

For C500, the decays time constants are 20 ps (92%) and 319 ps (8%) and for DCM, obtained time constants are 170 ps (96%) and 1.49 ns (4%). The slower water dynamics for hydrophobic DCM molecule is associated with the confinement of DCM in the hydrophobic region (oil tube) of the hexagonal mesophases in comparison to less hydrophobic C500 in the oil-water interface. Hence, more water can access the C500 probe in the excited state compared to DCM. In order to investigate the location and physical movement of C500 and DCM molecules within the LC during the course of the solvent relaxation, we have measured the fluorescence anisotropy of the probe molecules as shown in the insets of Fig. 4e-f. The fluorescence anisotropy decays depict rotational relaxation time constants of C500 and DCM in the liquid crystal are 325 ps and 653 ps respectively. The observed slower rotational time constants in case of DCM is consistent with the fact that DCM resides on the more compact oil phase while on the other hand C500 is more flexible on the oil-water interface. Hence, we can conclude that due to the hydrophobicity as well as the compact nature of the oil phase, the reduction of Pd complex takes place in the aqueous phase consequently the nanoparticles formed in the oil-water interface within the mesophases as proposed in the scheme 1.

**Electrochemical behavior.** As Pd-modified electrodes were demonstrated to be very active for ethanol electrooxidation in the alkaline medium, EOR was selected for electrocatalytic studies.<sup>10, 15, 16, 65, 66</sup> Fig. 5a and 5b depict the cyclic voltammogram (CV) of Pd-Nafion (the green solid line) and Pd/RGO-Nafion (the blue

solid line) in pure 1 M NaOH and voltammetric pattern associated with a characteristic feature of Pd electrodes which is consistent with earlier reports.<sup>15, 16, 43</sup> The Pd nanostructures embedded in a proton conducting phase, Nafion and RGO-Nafion matrix used as catalyst for the electrocatalytic oxidation of ethanol in an alkaline medium. Fig. 5a and b, shows superposition of the first cyclic voltammogram (black solid line curve) and the 100 cycle (red solid line curve) of Pd/Nafion and Pd/RGO-Nafion run in 1M NaOH containing 1M EtOH at a scan rate of 50 mVs<sup>-1</sup>.

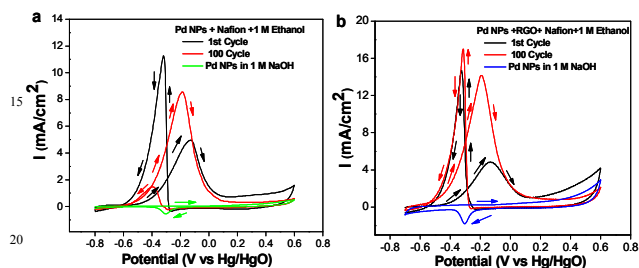


**Fig. 5** (a) Cyclic voltammograms of Pd NPs/Nafion in 1M NaOH (green solid line), superposition of the first (black solid line curve) and the 100<sup>th</sup> (red solid line curve) cyclic voltammetric runs associated with the electrocatalytic oxidation of 1 M EtOH in 1 M NaOH. (b) Cyclic voltammograms of Pd NPs/ RGO-Nafion in 1M NaOH (blue solid line), superposition of the first (black solid line curve) and the 100<sup>th</sup> (red solid line curve) cyclic voltammetric runs associated with the electrocatalytic oxidation of 1 M EtOH in 1 M NaOH. The working electrode was a glassy carbon disk modified with the Pd nanostructures. The reference electrode was an Hg/HgO (1 M KOH) electrode. The scan rate was 50 mVs<sup>-1</sup>.

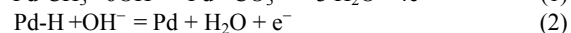
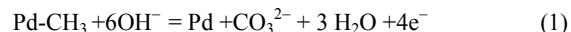
This voltammetric pattern is represented by two well-defined current peaks, one on the forward and the other on the reverse potential scans. The peak in the positive-going sweep corresponds to the ethanol oxidation activity, while the peak in the reverse sweep arises due to oxidation of both freshly adsorbed ethanol and adsorbed carbonaceous species formed before Pd-O blocking.<sup>67</sup> The forward scan peak current is related to the oxidation of freshly chemisorbed species issued from alcohol adsorption. The initial increment of current with number of triangular sweep of potential may be attributed to the generation of Pd-OH on the surface after each scan and development of channels of electron collection by rearrangement of the materials at the surface.<sup>42</sup> The oxygen desorption method is applicable to evaluate the electrochemically active surface area (ECSA) of Pd, the mass normalized ECSA were calculated for the two electrodes by computing the area under the cathodic peaks corresponding to the reaction of the Pd oxide monolayers. The data presented (within the parenthesis) reveal that ECSA of Pd/RGO-Nafion (192 m<sup>2</sup>g<sup>-1</sup>) is about 4.6 times greater than that of Pd/Nafion (40 m<sup>2</sup>g<sup>-1</sup>) electrode. This signifies that the former electrode is more exposed and available in the solvent environment for undergoing the reactions and hence shows increased surface area induced catalytic effect. The peak current and the onset potential of the faradaic current ( $E_{\text{onset}}$ ) on the forward scan indicate the electrocatalytic activity of the catalyst for EOR. The main quantitative parameters measured from these two voltammograms have been tabulated (Table 1). It can be

clearly seen from Table 1, the electroactivity (considering current per cm<sup>2</sup> of real area) of Pd/Nafion-RGO is higher than that of Pd/Nafion electrode. During the potential cycles, the  $E_{\text{onset}}$  shifts to a more negative potential (from -534 mV at the 1<sup>st</sup> cycle to -590 mV after 100 cycles, Table 1). It has to be noted that the stable cycle and 100 cycles are similar and used for further calculation of electrochemical parameters. A negative shift of  $E_{\text{onset}}$  underscores the enhancement in the kinetics of ethanol oxidation. Upon cycling, the peak current density is also modified: the forward anodic peak current density ( $I_f$ ) increased from 4.93 mA/cm<sup>2</sup> to 8.55 mA/cm<sup>2</sup> whereas the backward anodic peak current density ( $I_b$ ) decreased from 11.20 mA/cm<sup>2</sup> to 1.43 mA/cm<sup>2</sup>, leading to an increase of the ratio  $I_f/I_b$  from 0.44 to 5.98. This observation indicates no loss of catalyst and a relatively significant increase of electro-catalytic activity of the electrode material toward EOR during cycling. Indeed, a high  $I_f/I_b$  ratio indicates efficient oxidation of alcohol during the forward anodic scan, with little accumulation of carbonaceous residues. Thus it measures the tolerance power towards carbonaceous poisons and represents the capability of an electrode to remove the poisons either by possible chemical or electrochemical reactions occurring in the system.

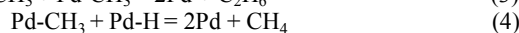
Table 1 Comparison of the electrochemical performance of Pd nanoparticle catalysts with nafion and reduced graphene oxides nanosheets modified nafion as supports for the oxidation of ethanol. The main characteristics measured from cyclic voltammograms associated with the electrocatalytic oxidation of 1 M EtOH in 1 M NaOH. The working electrode was a glassy carbon disc modified with the Pd nanostructures. The reference electrode was an Hg/HgO (1 M NaOH) electrode. The scan rate was 50 mV s<sup>-1</sup>. The current density is referred to the geometric area of the glassy carbon support.

Electrodes (after 100 cycles)	$I_f$ (mA. cm <sup>-2</sup> )	$I_b$ (mA. cm <sup>-2</sup> )	$I_f/I_b$	$E_{\text{onset}}$ (mV)	$I_f$ (mA. cm <sup>-2</sup> ). mg <sup>-1</sup>	$I_b$ (mA. cm <sup>-2</sup> ). mg <sup>-1</sup>
Pd/Nafion	8.55	1.43	5.98	-590	1745	292
Pd/RGO-Nafion	14.22	17.08	0.83	-622	5925	7166

Here the ratio of Pd/RGO-Nafion (0.83) is much smaller than that for Pd/Nafion (5.98). This plausibly fact that the spectroscopically determined intermediates like Pd-CH<sub>3</sub>, PdCH<sub>3</sub>CO, Pd-H etc are eliminated from the surface both by chemical and electrochemical reactions leading to opening of fresh metal surface. Since the rate of formation of these intermediates is greater for the electrode where peak current density is larger, the rate of elimination of these intermediate from the surface is also greater.<sup>44, 68</sup> If Pd-CH<sub>3</sub> or Pd-H is removed by electrochemical oxidation reaction the following reactions would take place:



In the contrary, if they remove chemically by the reactions:



The loss in  $I_f$  which corresponds to both faster dehydrogenation and slower decarboxaceous oxidation, is more than  $I_b$  which mainly contributed by surface-adsorbed carbonaceous oxidation. Thus the ratio,  $I_f/I_b$  is much smaller for Pd/RGO-Nafion than Pd/Nafion. This type of increased  $I_f/I_b$  ratio for a better electrode is a general phenomenon as observed in our previous study.<sup>44</sup> However, the increment in the forward anodic peak current density with respect to the backward anodic peak current density evaluated from potentiostatic experiments to identify the catalyst tolerance to carbonaceous species accumulation.<sup>15</sup> Similar results have been also obtained for the Pd-nanowires and palladium/gold nanostructures and such improvement in modified electrode characteristics might be attributed to some reorganization of the surface film<sup>10, 43</sup> or to a gradual cleaning of surfactant issue from the synthesis.<sup>15</sup> The similar electrochemical behavior upon cycling was observed with Pd NPs supported by RGO-Nafion (Pd/RGO-Nafion), assuming that the particular behavior is inherent to the metallic NPs. We checked the contribution of control RGO nanosheets during EOR and Fig. S5 shows the cyclic voltammograms for RGO nanosheets before and after addition of EtOH. However, the presence of RGO in combination with nafion as a support for Pd NPs influenced the values of the  $E_{\text{onset}}$ , the measured current density and the  $I_f/I_b$  ratio (Table 1). The onset of ethanol oxidation occurs at  $-0.590$  V for Pd/Nafion whereas it is  $-0.622$  V for Pd/RGO-Nafion suggesting that the electrocatalytic activity towards ethanol oxidation occurs more favorably in Pd/RGO-Nafion than in Pd/Nafion. It has been observed that in the first cycle, the peak current densities increased for both the forward and the backward scans and in contrast to Pd/Nafion, strikingly, backward current density increases after 100 cycles (Fig. 5b). According to the values extracted from the voltammograms, Pd NPs in nafion were the less active system compared to the Pd NPs in RGO-Nafion support, but they exhibited the best  $I_f/I_b$  ratio. An explanation for the high  $I_f/I_b$  ratio of Pd/Nafion could be that the nature of support RGO influences the adsorbed organic functions at the surface of the Pd NPs. The forward peak current density of Pd/Nafion and Pd/RGO-Nafion was  $8.55$  and  $14.22$   $\text{mA cm}^{-2}$ , respectively. The forward peak current of Pd/RGO-Nafion catalyst is 1.66 times that of the Pd/Nafion catalysts. Since, loading of the catalyst is different for the electrode, peak current densities of the CVs expressed also by dividing current densities ( $\text{mA cm}^{-2}$ ) with mass of Pd adsorbed per unit area of the surface ( $\text{mg}^{-1}$  of catalyst) as shown in Table 1. The influences of high surface area of RGO as support (Table 1) clearly highlight that RGO-Nafion support exhibited higher current density.<sup>69</sup> The comparison of the electrochemical performance of the present Pd nanostructure with other Pd based nanostructures under the comparable reaction conditions are listed in Table 2. Interestingly, the superiority of Pd/RGO-Nafion in terms of current density ( $7166 \text{ mA cm}^{-2} \text{ mg}^{-1}$ ) is obvious, being nearly 4.4 times higher than that of previously reported Pd nanowires ( $1327 \text{ mA cm}^{-2} \text{ mg}^{-1}$ ) synthesized in hexagonal mesophases as shown in Table 2).<sup>15</sup> In fact, the Pd/RGO-Nafion catalyst has superior catalytic activity with high energy density among these Pd catalysts. This may be due to synergistic effect assembled Pd

nanoparticles and reduced graphene oxides nanosheets that can efficiently promote the breaking of C-C bond of ethanol and enhance the oxidation of ethanol. In contrast to Pd assembly, the Pd NPs synthesized within micelles are not active due to presence of surfactant molecules which limit the accessibility of Pd electrocatalyst on the electrode.

**Table 2** Comparison of the electrochemical performance of Pd nanostructured electrocatalysts for the ethanol oxidation.

Electrode	$E_{\text{onset}}$ , mV/SCE	$E_f$ , mV/SCE	$E_b$ , mV/SCE	$I_f$ , $\text{mA cm}^{-2}$	$I_f$ , $\text{mA cm}^{-2} \text{ mg}^{-1}$ of Pd	Reference
Pd/Nafion	-590	-185	-382	8.55	1745	This work
Pd/RGO-Nafion	-622	-186	-312	14.22	5925	This work
Commercial Pd black catalyst	-550	~ -200	~ -301	0.65	-	8
Tetrahedral Pd nanocrystal	-590	-219	~ -305	3.83	-	8
Pd/Nf-graphene	-600	-	-	0.56	-	2
C-Pd Nanoballs/ Nafion	-550	-151	-296	-	-	16
Pd nanowires /Nafion	-664	-166	-278	-	1327	15
CNT-Pd/Nafion	-564	-242	-451	-	364	37
CNT-Pd/Nafion	-670	-245	-332	-	3540	37
C-Pd	-680	-209	~ -310	-	63	63
C-Pd	-579	-219	~ -360	-	42	64
C-Pd	-619	-203	~ -330	-	85	64

The catalyst stability as a function of time is also important for its practical application in direct ethanol fuel cells. The stability of the catalytic performance was then investigated by chronoamperometric (CA) measurements where the current density-time ( $I$  vs  $t$ ) curves at constant potentials were recorded as shown in Fig 6.

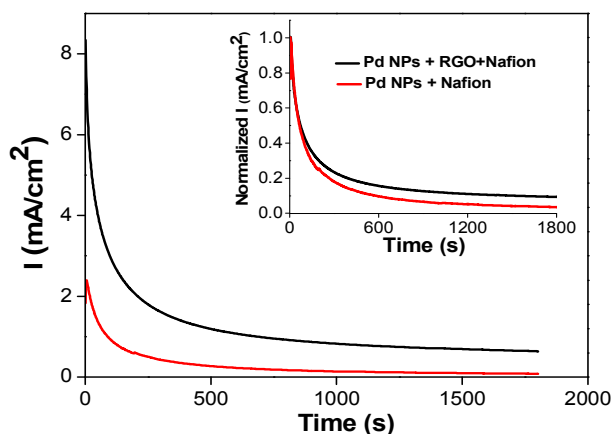


**Fig. 6** Chronoamperometric curves for the ethanol electrooxidation at  $-0.30$  V vs Hg/HgO on a glassy carbon electrode modified with Pd/Nafion (black curve) and Pd/RGO-Nafion (red curve). The solution was  $1 \text{ M NaOH} + 1 \text{ M EtOH}$ . Inset: the comparison of chronoamperometric response of Pd/Nafion and Pd/RGO-Nafion at normalized current ( $I$ ).

The CA experiments were measured in  $1 \text{ M NaOH}$  with  $1 \text{ M ethanol}$  solution under a constant potential of  $0.3 \text{ V}$  for  $1600 \text{ s}$ . In

the first several minutes, both catalysts exhibited a pronounced current decay, which could be caused by the accumulation of poisonous intermediates.<sup>70</sup> The current density decayed in the first 500 s and attained a steady state thereafter, indicating that these Pd NPs form very stable film on glassy carbon electrode surface and also exhibit stable electrocatalytic performance towards EOR. After 500 s, the order of activity in the CA tests was similar with the activity order in the CV measurements: Pd/RGO-Nafion catalyst exhibited the highest limiting as well as the initial current, showing the highest activity than the Pd/Nafion catalysts. Moreover, Pd/RGO-Nafion exhibits a lower degradation rate during the reaction progress, which demonstrates its improved stability for ethanol electro-oxidation. The enhanced EOR activity and stability for the Pd/RGO-Nafion electrocatalyst compared to Pd/Nafion are probably related to the surface structure and properties of the reduced graphene oxide nanosheets. The chronoamperometric response confirms that the RGO nanosheets help in the effective dispersion of the Pd NPs, facilitating an easier access of ethanol molecules to the catalytic sites. Additionally, the RGO nanosheets having the holes, oxygen, carbon vacancies and defects which are generated as partial oxidation produces sheets with graphitic domains. This may efficiently introduce chemically active sites for use in catalytic reactions and also act as anchoring sites for deposition of metal NPs.<sup>49, 71</sup> Furthermore, it is also beneficial to prevent the metal nanoclusters from coalescence because of homogeneous dispersion of the Pd NPs on the support and consequently increases the accessibility of metal catalyst during electrocatalytic reaction.<sup>72</sup> Hence, the addition of reduced GO nanosheets as a support could remarkably improve the stability of Pd nanostructure for EOR, which is crucial for a practical catalyst.

#### 4. Conclusions

In summary, we have successfully developed a facile and reproducible method for the high-yield synthesis of assembled Pd nanostructures in hexagonal mesophases by photoreduction. The as-prepared electrocatalysts supported with RGO nanosheets exhibit dramatically enhanced activity and stability for ethanol electrooxidation in alkaline conditions, demonstrating that they can be used as effective electrocatalysts for direct ethanol fuel cells. Hence, RGO-Nafion support can eventually affect the overall quality of the electro-catalytic activity of Pd nanostructure with high current density and more negative onset potentials of the faradaic current which is also supported with 4.6 times higher ECSA in comparison to Nafion alone. In light of the important role of nanostructures in catalysis and their facile synthetic process, the as-synthesized catalysts may also find suitable applications in other fuel cells relevant reactions, such as formic acid oxidation, methanol oxidation and oxygen reduction reaction, etc. The coupling of graphene oxide nanosheets with metal nanostructures leads to superior activity. The use of graphene nanosheets synthesized by a scalable, clean approach without using any chemical reducing agent via low-cost approach may encourage real-world applications in the field of fuel cells. Moreover, the electrochemical performance of Pd based materials is strongly dependent on individual components and their interactions with each other. Hence, further studies are required to understand the underlying complex interactions between Pd catalyst and graphene based support. Finally, exploration of novel Pd assembled nanostructures supported with graphene oxide nanosheets and nafion can be extended to design other advanced materials for a promising anode catalyst in DEFCs.

**Acknowledgements.** S. G. acknowledges Marie Curie Cofund, RBUCE-UP (Research Based University Chairs of Excellence of Paris) and PRES UniverSud Paris for financial support. P. K. and S. C. thanks the Council of Scientific and Industrial Research (CSIR, India) for fellowships. S.K.P. thanks the Department of Science and Technology (DST, India) for financial grants. The authors gratefully acknowledge C'Nano Ile de France and Université Paris-Sud (ERM project) for financial support for the Cobalt-60 panoramic gamma source.

#### Notes and References

- <sup>a</sup>Department of Chemical, Biological and Macromolecular Sciences, S. N. Bose National Centre for Basic Sciences, Block JD, Sector III, Salt Lake, Kolkata 700 098, India  
<sup>b</sup>Laboratoire de Chimie Physique, UMR 8000-CNRS, Université Paris-Sud, 91405 Orsay Cedex, France  
<sup>c</sup>CNRS, Laboratoire de Chimie Physique, UMR 8000, 91405 Orsay, France  
<sup>d</sup>Sorbonne Universités, UPMC Univ. Paris 06, UMR 7197-CNRS, Laboratoire de Réactivité de Surface, F-75005 Paris, France  
<sup>e</sup>Physical Chemistry Section, Department of Chemistry, Jadavpur University, Kolkata, 700 032, India

\*Corresponding author, E-mail: [ghosh.srabanti@mail.com](mailto:ghosh.srabanti@mail.com), [srabanti.ghosh@bose.res.in](mailto:srabanti.ghosh@bose.res.in)

† Electronic Supplementary Information (ESI) available: Additional information, Polarized light micrographs, FTIR spectra, TEM and HRTEM images and CV pattern. See DOI: 10.1039/b000000x/

1. A. S. Arico, P. Bruce, B. Scrosati, J.-M. Tarascon and W. van Schalkwijk, *Nat Mater*, 2005, **4**, 366-377.
2. Q. Zhang, E. Uchaker, S. L. Candelaria and G. Cao, *Chem. Soc. Rev.*, 2013, **42**, 3127-3171.
3. P. Kar, S. Sardar, E. Alarousu, J. Sun, Z. S. Seddigi, S. A. Ahmed, E. Y. Danish, O. F. Mohammed and S. K. Pal, *Chem. Eur. J.*, 2014, **20**, 10475-10483.
4. X. Cheng, Z. Shi, N. Glass, L. Zhang, J. Zhang, D. Song, Z.-S. Liu, H. Wang and J. Shen, *J. Power Sources* 2007, **165**, 739-756.
5. E. Christoffersen, P. Liu, A. Ruban, H. L. Skriver and J. K. Nørskov, *J. Catal.*, 2001, **199**, 123-131.
6. C. Bianchini and P. K. Shen, *Chem. Rev.*, 2009, **109**, 4183-4206.
7. P. S. Roy, J. Bagchi and S. K. Bhattacharya, *Catal Sci Technol*, 2012, **2**, 2302-2310.
8. N. Tian, Z.-Y. Zhou, N.-F. Yu, L.-Y. Wang and S.-G. Sun, *J. Am. Chem. Soc.*, 2010, **132**, 7580-7581.
9. X. Huang, Y. Li, Y. Li, H. Zhou, X. Duan and Y. Huang, *Nano Lett.*, 2012, **12**, 4265-4270.
10. F. Ksar, L. Ramos, B. Keita, L. Nadjo, P. Beaunier and H. Remita, *Chem. Mater.*, 2009, **21**, 3677-3683.
11. C. Koenigsmann, A. C. Santulli, E. Sutter and S. S. Wong, *ACS Nano*, 2011, **5**, 7471-7487.
12. X. Huang, S. Tang, X. Mu, Y. Dai, G. Chen, Z. Zhou, F. Ruan, Z. Yang and N. Zheng, *Nat Nano*, 2011, **6**, 28-32.
13. P. S. Roy and S. K. Bhattacharya, *Catal Sci Technol*, 2013, **3**, 1314-1323.
14. H. Zhang, M. Jin, Y. Xiong, B. Lim and Y. Xia, *Acc. Chem. Res.*, 2012, **46**, 1783-1794.
15. F. Ksar, G. Surendran, L. Ramos, B. Keita, L. Nadjo, E. Prouzet, P. Beaunier, A. Hagège, F. Audonnet and H. Remita, *Chem. Mater.*, 2009, **21**, 1612-1617.
16. G. Surendran, F. Ksar, L. Ramos, B. Keita, L. Nadjo, E. Prouzet, P. Beaunier, P. Dieudonné, F. Audonnet and H. Remita, *J. Phys. Chem. C*, 2008, **112**, 10740-10744.
17. L.-F. Zhang, S.-L. Zhong and A.-W. Xu, *Angew. Chem. Int. Ed.*, 2013, **52**, 645-649.
18. S. Guo, S. Dong and E. Wang, *Energy Environ Sci*, 2010, **3**, 1307-1310.

19. P. K. Shen and C. Xu, *Electrochem. Commun.*, 2006, **8**, 184-188.
20. T. Hegmann, H. Qi and V. Marx, *J. Inorg. Organomet. Polym.*, 2007, **17**, 483-508.
21. G. Surendran, G. Apostolescu, M. Tokumoto, E. Prouzet, L. Ramos, P. Beaunier, P. J. Kooyman, A. Etcheberry and H. Remita, *Small*, 2005, **1**, 964-967.
22. K. Kanie and T. Sugimoto, *J. Am. Chem. Soc.*, 2003, **125**, 10518-10519.
23. S. Kubo, R. Taguchi, S. Hadano, M. Narita, O. Watanabe, T. Iyoda and M. Nakagawa, *ACS Appl. Mater. Interfaces*, 2013, **6**, 811-818.
24. J. Mirzaei, M. Urbanski, H.-S. Kitzerow and T. Hegmann, *ChemPhysChem*, 2014, **15**, 1381-1394.
25. V. J. Anderson, E. M. Terentjev, S. P. Meeker, J. Crain and W. C. K. Poon, *Eur. Phys. J. E*, 2001, **4**, 11-20.
26. P. G. Petrov and E. M. Terentjev, *Langmuir*, 2001, **17**, 2942-2949.
27. S. P. Meeker, W. C. K. Poon, J. Crain and E. M. Terentjev, *Phys. Rev. E*, 2000, **61**, R6083-R6086.
28. G. S. Attard, P. N. Bartlett, N. R. B. Coleman, J. M. Elliott, J. R. Owen and J. H. Wang, *Science*, 1997, **278**, 838-840.
29. G. S. Attard, J. M. Corker, C. G. Göltner, S. Henke and R. H. Templer, *Angew. Chem. Int. Ed.*, 1997, **36**, 1315-1317.
30. A. Lehoux, L. Ramos, P. Beaunier, D. B. Uribe, P. Dieudonné, F. Audonnet, A. Etcheberry, M. José-Yacamán and H. Remita, *Adv. Funct. Mater.*, 2012, **22**, 4900-4908.
31. E. Pena dos Santos, M. S. Tokumoto, G. Surendran, H. Remita, C. Bourgaux, P. Dieudonné, E. Prouzet and L. Ramos, *Langmuir*, 2005, **21**, 4362-4369.
32. G. Surendran, M. S. Tokumoto, E. Pena dos Santos, H. Remita, L. Ramos, P. J. Kooyman, C. V. Santilli, C. Bourgaux, P. Dieudonné and E. Prouzet, *Chem. Mater.*, 2005, **17**, 1505-1514.
33. T. Redjala, G. Apostolecu, P. Beaunier, M. Mostafavi, A. Etcheberry, D. Uzio, C. Thomazeau and H. Remita, *New J. Chem.*, 2008, **32**, 1403-1408.
34. P. F. Siril, L. Ramos, P. Beaunier, P. Archirel, A. Etcheberry and H. Remita, *Chem. Mater.*, 2009, **21**, 5170-5175.
35. Ghosh S., Kouamé N. A., Ramos L, Remita S, AlDazzi S, Deniset-Besseau A, Beaunier P, Goubard F, Aubert P and R. H., *Nat Mater*, 2015, **10**, DOI: 10.1038/NMAT4220.
36. S. Ghosh, H. Remita, L. Ramos, A. Dazzi, A. Deniset-Besseau, P. Beaunier, F. Goubard, P.-H. Aubert, F. Brisset and S. Remita, *New J. Chem.*, 2014, **38**, 1106-1115.
37. N. Mackiewicz, G. Surendran, H. Remita, B. Keita, G. Zhang, L. Nadjo, A. Hagège, E. Doris and C. Mioskowski, *J. Am. Chem. Soc.*, 2008, **130**, 8110-8111.
38. R. Krishna, E. Titus, O. Okhay, J. C. Gil, J. Ventura, E. V. Ramana and J. J. A. Gracio, *Int. J. Electrochem. Sci.*, 2014, **9**, 4054-4069.
39. H. T. Zheng, Y. Li, S. Chen and P. K. Shen, *J. Power Sources*, 2006, **163**, 371-375.
40. P. Kanninen, M. Borghei, V. Ruiz, E. I. Kauppinen and T. Kallio, *Int J Hydrogen Energy* 2012, **37**, 19082-19091.
41. M. A. Newton, C. Belver-Coldeira, A. Martinez-Arias and M. Fernandez-Garcia, *Nat Mater*, 2007, **6**, 528-532.
42. H. L. Xin, J. A. Mundy, Z. Liu, R. Cabezas, R. Hovden, L. F. Kourkoutis, J. Zhang, N. P. Subramanian, R. Makharia, F. T. Wagner and D. A. Muller, *Nano Lett.*, 2011, **12**, 490-497.
43. S. Ghosh, A.-L. Teillout, D. Floresyona, P. d. Oliveira, A. Hagège and H. Remita, *Int J Hydrogen Energy* 2015, doi.10.1016/j.ijhydene.2015.01.101.
44. P. Mukherjee, P. S. Roy, K. Mandal, D. Bhattacharjee, S. Dasgupta and S. K. Bhattacharya, *Electrochim. Acta*, 2015, **154**, 447-455.
45. Y. Zhao, L. Zhan, J. Tian, S. Nie and Z. Ning, *Electrochim. Acta*, 2011, **56**, 1967-1972.
46. E. Antolini, *Appl. Catal., B* 2012, **123-124**, 52-68.
47. Y. Li, H. Wang, L. Xie, Y. Liang, G. Hong and H. Dai, *J. Am. Chem. Soc.*, 2011, **133**, 7296-7299.
48. Y. Liang, Y. Li, H. Wang, J. Zhou, J. Wang, T. Regier and H. Dai, *Nat Mater*, 2011, **10**, 780-786.
49. E. Yoo, T. Okata, T. Akita, M. Kohyama, J. Nakamura and I. Honma, *Nano Lett.*, 2009, **9**, 2255-2259.
50. C. Huang, C. Li and G. Shi, *Energy Environ Sci*, 2012, **5**, 8848-8868.
51. S. Stankovich, D. A. Dikin, G. H. B. Dommett, K. M. Kohlhaas, E. J. Zimney, E. A. Stach, R. D. Piner, S. T. Nguyen and R. S. Ruoff, *Nature*, 2006, **442**, 282-286.
52. W. S. Hummers and R. E. Offeman, *J. Am. Chem. Soc.*, 1958, **80**, 1339-1339.
53. D. Li, M. B. Muller, S. Gilje, R. B. Kaner and G. G. Wallace, *Nat Nano*, 2008, **3**, 101-105.
54. M. L. Horng, J. A. Gardecki, A. Papazyan and M. Maroncelli, *J. Phys. Chem.*, 1995, **99**, 17311-17337.
55. S. Batabyal, T. Mondol, S. Choudhury, A. Mazumder and S. K. Pal, *Biochimie*, 2013, **95**, 2168-2176.
56. J. Bagchi and S. K. Bhattacharya, *J. Power Sources* 2007, **163**, 661-670.
57. M. Manfait, A. J. P. Alix and C. Kappenstein, *Inorg. Chim. Acta*, 1981, **50**, 147-152.
58. K. H. S. Kung and K. F. Hayes, *Langmuir*, 1993, **9**, 263-267.
59. K. R. Gopidas, J. K. Whitesell and M. A. Fox, *Nano Lett.*, 2003, **3**, 1757-1760.
60. M. N. Nadagouda and R. S. Varma, *Green Chem.*, 2008, **10**, 859-862.
61. G. Wang, J. Yang, J. Park, X. Gou, B. Wang, H. Liu and J. Yao, *J. Phys. Chem. C*, 2008, **112**, 8192-8195.
62. F. Dehouche, P. Archirel, H. Remita, N. Brodie-Linder and A. Traverse, *RSC Advances*, 2012, **2**, 6686-6694.
63. S. Choudhury, S. Batabyal, T. Mondol, D. Sao, P. Lemmens and S. K. Pal, *Chem Asian J*, 2014, **9**, 1395-1402.
64. R. Sarkar, A. K. Shaw, M. Ghosh and S. K. Pal, *J. Photochem. Photobiol., B* 2006, **83**, 213-222.
65. C. Xu, P. k. Shen and Y. Liu, *J. Power Sources* 2007, **164**, 527-531.
66. M. Grdeń, M. Łukaszewski, G. Jerkiewicz and A. Czerwiński, *Electrochim. Acta* 2008, **53**, 7583-7598.
67. R. Mancharan and J. B. Goodenough, *J. Mater. Chem.*, 1992, **2**, 875-887.
68. K. Mandal, D. Bhattacharjee, P. S. Roy, S. K. Bhattacharya and S. Dasgupta, *Appl. Catal., A*, 2015, **492**, 100-106.
69. X. Yang, Q. Yang, J. Xu and C.-S. Lee, *J. Mater. Chem.*, 2012, **22**, 8057-8062.
70. A. Kabbabi, R. Faure, R. Durand, B. Beden, F. Hahn, J. M. Leger and C. Lamy, *J. Electroanal. Chem.*, 1998, **444**, 41-53.
71. K. Erickson, R. Ermi, Z. Lee, N. Alem, W. Gannett and A. Zettl, *Adv. Mater.*, 2010, **22**, 4467-4472.
72. G. Prieto, J. Zečević, H. Friedrich, K. P. de Jong and P. E. de Jongh, *Nat Mater*, 2013, **12**, 34-39.

Synthesis of self assembled Pd nanostructures supported with reduced graphene oxides nanosheets as promising electrocatalyst for the electrooxidation of ethanol.

